

Cosmic-Ray Positrons Strongly Constrain Leptophilic Dark Matter

Isabelle John^{1,*} and Tim Linden^{1,†}

¹*Stockholm University and The Oskar Klein Centre for Cosmoparticle Physics, Alba Nova, 10691 Stockholm, Sweden*

Cosmic-ray positrons have long been considered a powerful probe of dark matter annihilation. In particular, myriad studies of the unexpected rise in the positron fraction have debated its dark matter or pulsar origins. In this paper, we instead examine the potential for extremely precise positron measurements by AMS-02 to probe hard leptophilic dark matter candidates that *do not* have spectral features similar to the bulk of the observed positron excess. Utilizing a detailed cosmic-ray propagation model that includes a primary positron flux generated by Galactic pulsars in addition to a secondary component constrained by Helium and proton measurements, we produce a robust fit to the local positron flux and spectrum. We find no evidence for a spectral bump correlated with leptophilic dark matter, and set strong constraints on the dark matter annihilation cross-section that fall below the thermal annihilation cross-section for dark matter masses below 60 GeV and 380 GeV for annihilation into $\tau^+\tau^-$ and e^+e^- , respectively, in our default model.

I. INTRODUCTION

The AMS-02 experiment, onboard the International Space Station, has provided extremely precise observations of the flux, composition and spectrum of local cosmic-rays [1]. These data yield new insights into the energetics of the Galaxy’s most powerful sources, and the properties of Galactic transport. Additionally, searches for unexpected spectral features can potentially provide evidence for new physics, such as anisotropic diffusion or even dark matter annihilation.

Notably, AMS-02 observations have built upon data by the PAMELA observatory [2] and earlier instruments [3, 4], to provide strong evidence for a steep rise in the positron fraction above 10 GeV, and a drop-off at 300 GeV [5]. The two most plausible explanations for this excess are pulsars, *e.g.*, [6–10], and annihilating dark matter particles, *e.g.*, [11–19]. Recently, observations of bright γ -ray emission surrounding young and middle aged pulsars (*e.g.*, Geminga, Monogem, and a handful of younger HAWC and H.E.S.S. sources that are now named TeV halos [20–27]), which are powered by the efficient acceleration of high-energy electrons, have favoured the pulsar interpretation [6–10, 28–33]. At the same time, dark matter models have come into tension with γ -ray limits from several targets, including dwarf spheroidal galaxies [13, 34–39].

In this paper, we consider the constraints that can be placed on dark matter in scenarios that attribute the bulk of the rising positron fraction above 10 GeV to Galactic pulsars. We make use of the high-statistical precision of the AMS-02 data to calculate strong constraints on dark matter annihilation into highly-peaked leptonic final states, which have spectra that are inconsistent with the high-energy positron spectrum. A schematic example of the scenario we examine is shown in Figure 1: At lower energies, the positron flux is dominated by secondary positrons produced by protons and Helium nuclei, while at higher energies, most positrons are produced in electron-positron pairs accelerated by pulsars. Against this background, our analysis probes a subdominant contribution from annihilating dark matter.

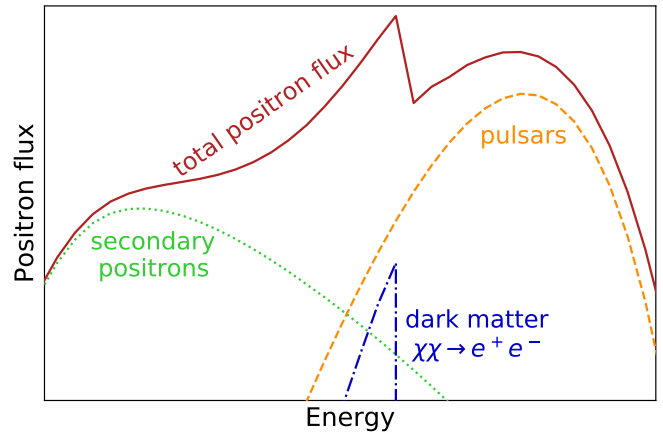


FIG. 1. A schematic diagram of the scenario we examine. We model a positron flux that includes a primary contribution from pulsars, secondary contributions from the hadronic interactions of primary cosmic-rays, and a highly peaked contribution from dark matter annihilation into leptonic final states, which we attempt to constrain.

This result builds on a similar analysis by Bergström *et al.* (2013) [40]. Their work tests two discrete models for the astrophysical background, as well as contributions from dark matter particles between 5–300 GeV annihilating into leptonic final states ($\tau^+\tau^-$, $\mu^+\mu^-$, $e^+e^- \gamma$ and e^+e^-). Their strongest limits are obtained for the direct e^+e^- channel, where they set upper limits on the dark matter annihilation cross section of about $10^{-28} \text{ cm}^3 \text{ s}^{-1}$ at 5 GeV and about $10^{-25} \text{ cm}^3 \text{ s}^{-1}$ at 250 GeV.

In this paper, we update and improve on the Bergström *et al.* results in three ways: (1) Our analysis utilizes a larger dataset provided by the the latest AMS-02 measurements of positron, proton, and Helium fluxes [5, 41–43]. (2) We use the cosmic-ray propagation code Galprop [44] to create a full cosmic-ray propagation model for the positron, proton and Helium data. Our fit allows a large variety of parameters, such as the diffusion and particle injection spectra in the fit to float, while Bergström *et al.* build their background from a handful of pre-defined Galprop models. (3) We implement a new solar modulation model [45] to describe the effect of solar activity on low-energy cosmic-ray particles, rather than approximating solar modulation by a force-field potential.

* isabelle.john@fysik.su.se, ORCID: orcid.org/0000-0003-2550-7038

† linden@fysik.su.se, ORCID: orcid.org/0000-0001-9888-0971

The paper is outlined as follows: In Section II, we describe the methodology of this analysis and explain the data selection (Sec. II A), the computational model (Sec. II B), the dark matter model (Sec. II C) and the statistical analysis (Sec. II D). The results are presented in Section III, and our conclusions are discussed in Section IV.

II. METHODOLOGY

In this section, we describe our selection of the AMS-02 data, and present our methodology for constructing astrophysical models that fit this data. We also describe our statistical analysis of constraining the dark matter contribution.

Our analysis generally proceeds as follows. To compute the dark matter limits, we perform a fit of the positron, proton and Helium data from AMS-02 to constrain the parameters of our astrophysical model. While the high-energy positron spectrum is dominated by primary positrons that are created by pulsars as electron-positron pairs, low-energy positrons are produced as secondaries from proton interactions with a subdominant contribution from Helium (about 10%). After obtaining an astrophysical model for the positron flux in the absence of dark matter, we add a dark matter contribution and compute the 95% confidence upper limit on the dark matter annihilation rate. Notably, we allow critical astrophysical parameters to be re-fit for each dark matter mass and cross-section, producing a more realistic constraint on the dark matter contribution. In the following sections, the procedure is described in more detail.

A. Data Selection

Our analysis takes advantage of the recently published AMS-02 data for positrons [5], protons [41, 42], and Helium [43]. A summary of the data sets is given in Table I. We note that our constraints on leptophilic dark matter only directly depend on our analysis of the positron data, but we include protons and Helium in the astrophysical model to obtain better constraints on the model parameters. We also note that protons and Helium have the same electric charge as positrons, which decreases the relative uncertainties from solar modulation.

For positrons, we consider energies in the range from 2 to 1000 GeV in our fit. We do not include energies below 2 GeV due to their large uncertainties, especially coming from solar modulation [46], and because the dark matter contribution is small at low energies. To achieve the best statistical precision, we take a large dataset that includes the AMS-02 data from May 2011 to November 2017 [5]. For protons, we consider energies in the range from 2 to 1800 GeV, for which we combine two data sets: From 2 to 60 GeV, AMS-02 provides time-dependent data [41], and we select the data from February 2015 to May 2017 (Bartels rotations 2477–2506), after the polarity flip of the solar magnetic field was completed, to avoid additional uncertainties from the effects of the solar modulation. At energies from 60 to 1800 GeV, we use the

Particle	Energy range [GeV]	Time range	Ref.
Positrons	2 – 1000	May 2011 – Nov. 2017	[5]
Protons	2 – 60	Feb. 2016 – May 2017	[41]
	60 – 1800	May 2011 – Nov. 2013	[42]
Helium	2 – 1000	May 2011 – Nov. 2013	[43]

TABLE I. AMS-02 data sets used in this analysis. Since our solar modulation model is time-dependent, we are able to utilize datasets from different time periods.

time-independent data in [42], recorded from May 2011 to November 2013. At these energies, the effect of solar modulation is negligible. For Helium, we consider the energy range from 2 GeV to 1000 GeV and use the time-independent data from May 2011 to November 2013, which includes both ^3He and ^4He [43]. As the conversion from rigidity to energy depends on the number of nucleons, we estimate the ratio of ^3He to ^4He in this flux by linearly extrapolating the ratio given in [47] to fluxes at higher energies.

B. Computational Model

To simulate galactic cosmic-ray propagation, we use Galprop v.5.6 [44, 48–54], a state-of-the-art tool to compute cosmic-ray propagation, that takes into account numerous processes, such as diffusion, spallation, energy losses and reacceleration. For our analysis, it is sufficient to solve the propagation equation in 2D, and to include only cosmic-ray contributions up to ^4He , while ignoring heavier nuclei.

Galprop simulations begin by injecting a significant flux of primary cosmic-rays (most importantly for our analysis, protons and ^4He) following the standard supernova spatial distribution [55]. The subsequent propagation and hadronic interactions of these primary particles produce a secondary flux, which includes more protons as well as new components (most importantly, positrons and ^3He). We supplement these contributions from supernovae with an additional component of primary electrons and positrons powered by pulsar activity, as described below.

We tune the following Galprop parameters in our model. We model the diffusion spectrum with a diffusion coefficient D_0 set at a reference rigidity of 4 GV and a diffusion break D_{break} , where δ_1 and δ_2 are the spectral indices below and above the break, respectively. The proton injection spectrum is modelled by three free parameters, including two spectral indices and a critical energy describing their transition. This break primarily affects the lowest energy protons and positrons. Similarly, for Helium we introduce a spectral break and spectral indices γ_1^{He} and γ_2^{He} below and above the break, respectively. At higher energies, most of the positron contribution comes from pulsars, where the free parameters are the spectral index γ_{psr} , the cutoff energy $E_{\text{cut}}^{\text{psr}}$ of the spectrum and the pulsar formation rate \dot{N}_{100} (discussed below). Reacceleration is taken into account by the Alfvén velocity which is most important for positrons and has a smaller effect on protons. The convection velocity v_{conv} and the solar modulation parameters (ϕ_0 and ϕ_1 , discussed below) are significant at

Parameter	Value
Local dark matter density, ρ_{loc} [GeV/cm ³]	0.4
Dark matter halo core radius [kpc]	20
Magnetic field at Earth [μG]	5.7

TABLE II. List of parameters that are fixed in the model.

lower energies. Lastly, there is an overall normalization of the spectra computed by Galprop which is related to uncertainties in the Milky Way supernova rate [56].

A particularly important parameter in the model is the halo height, z . The dark matter contribution is proportional to the halo height, and therefore we examine this parameter individually. We compute the astrophysical model for two fixed values of the halo height: setting $z = 5.6$ kpc as a standard height (default model), and $z = 3$ kpc as the lower limit on the halo height (small-height model) [57–59].

In our model, we introduce pulsars as a new source of primary positrons by modifying the Galprop code. For this, we adopt the standard pulsar distribution profile from [60, 61], to obtain the 3-dimensional pulsar distribution in the Galaxy,

$$\rho(R) = 64.6 \text{ kpc}^{-4.35} R^{2.35} \exp\left[\frac{-R}{R_0}\right] \exp\left[\frac{-|z|}{z_0}\right], \quad (1)$$

where z is the halo height of the Milky Way, and $R_0 = 1.528$ kpc and $z_0 = 0.330$ kpc. We model the e^+e^- spectrum from pulsars as a power-law with an exponential cutoff [6],

$$\frac{dN}{dE} \approx C \left(\frac{E}{\text{GeV}}\right)^{-\gamma_{\text{psr}}} \exp\left[\frac{-E}{E_{\text{cut}}^{\text{psr}}}\right] (\text{GeV s})^{-1}, \quad (2)$$

where γ_{psr} is the spectral index and $E_{\text{cut}}^{\text{psr}}$ the cutoff energy. For the normalization, we calculate C such that the average total pulsar spindown luminosity is 10^{49} erg [6], and the average efficiency for the conversion of pulsar spindown power into e^+e^- pairs is 1%. In our model, we let γ_{psr} , $E_{\text{cut}}^{\text{psr}}$ and \dot{N}_{100} float, fitting the spectrum and normalization of the pulsar contribution.

Cosmic-ray measurements are affected by the heliosphere of the Sun, causing particle losses at low energies ($\lesssim 10$ GeV). This effect strongly depends on the orientation of the solar magnetic field and solar activity. Often (*e.g.*, as in [40]), the solar modulation is approximated by a force-field potential [46]. Here, we implement the solar modulation model from [45] that takes into account the time-, charge- and rigidity dependence of the solar modulation. In the solar modulation model, we choose time periods that match the data analysis periods from AMS-02, and keep the parameters ϕ_0 and ϕ_1 , that describe the heliospheric potential, as free parameters.

Additionally, there are several important parameters that we fix to their standard Galprop values. Most notably, we utilize a Galactic magnetic field model based on Model C of Ref. [62], utilizing the re-fit value for the radial scale height of the regular magnetic field of 13 kpc. This model yields a magnetic field at the solar position of $5.7 \mu\text{G}$. All parameters for our astrophysical models can be found in Table III for the default model and small-height model.

C. Dark Matter Model

For the dark matter model, we assume a local dark matter density of 0.4 GeV/cm^3 and a core radius of the dark matter halo of 20 kpc (*c.f.* [63]), see Table II, and describe the dark matter distribution in the Galaxy using a generalized NFW profile [64]. We utilize a non-standard NFW slope of 0.5, but note that this choice has almost no effect on the local dark matter annihilation rate – producing limits that are more conservative by a few percent. We consider four different leptophilic final states for the dark matter annihilation: $\chi\chi \rightarrow \tau^+\tau^-$, $\chi\chi \rightarrow \mu^+\mu^-$, $\chi\chi \rightarrow e^+e^-$, and $\chi\chi \rightarrow \phi\phi \rightarrow e^+e^-e^+e^-$, where ϕ is a light mediator. For the $\tau^+\tau^-$, and $\mu^+\mu^-$ final states, we use dark matter spectra obtained with DarkSUSY v.5.1.1 [65]. For the $e^+e^-e^+e^-$ and e^+e^- states, we utilize analytic calculations of the dark matter spectrum that we directly implement in Galprop. Specifically, in the $e^+e^-e^+e^-$ case, the contribution to the differential positron flux is constant and integrates to the dark matter mass over the full energy range, following a similar calculation in [66]. The e^+e^- final state is represented by a delta function and we smear out the contribution to the positron flux over the neighbouring energy bins in Galprop.

D. Statistical Analysis

To calculate the best-fit values for our model parameters, we use two minimization codes: `pyMultinest v.2.10` [67–70] and `iMinuit v.1.4.3`. [71, 72].

We create our astrophysical model in two steps: First we fit positrons and protons over a wide range of parameters. For this we use Multinest as it can handle the large number of free parameters well and is reliable at finding the global minimum. Then we add Helium to the fit and re-fit the previous parameters together with the Helium injection spectrum. For this, we use iMinuit as it finds the exact values of the minimum more precisely than Multinest. Because their contribution to the positron flux is negligible, we do not include nuclei larger than Helium in Galprop.

Throughout our analysis, we compare our model with the AMS-02 particle fluxes in multiple energy bins. We note that the AMS-02 data includes uncertainties that stem from both statistical and systematic errors. The systematic errors are likely to be correlated between energy bins, but to date, the AMS-02 collaboration has not released a covariance matrix that accounts for the correlation between systematic errors in nearby energy bins. Thus, in this paper, we treat the systematic and statistical errors in each bin independently, adding them in quadrature. This leads to an overestimate of the AMS-02 error budget, and allows our models to achieve goodness of fit values less than 1. Notably, however, this preserves the same minimum value for the best-fit, and still allows us to compare models in terms of their $\Delta\chi^2$.

For the first step, we use Multinest to fit the astrophysical parameters corresponding to proton and positron propagation discussed in Section II B. We show the intermediate results of this procedure in Appendix A.

Parameter	Range	default model (5.6 kpc)	small-height model (3 kpc)
Diffusion coefficient, D_0 [cm^2/s]	$10^{28} - 10^{30}$	$1.636 \cdot 10^{28}$	$1.679 \cdot 10^{28}$
Diffusion spectrum break, D_{break} [MV]	$10^3 - 1.4 \cdot 10^4$	$6.067 \cdot 10^3$	$6.965 \cdot 10^3$
Spectral index below break, δ_1	0.01 – 0.61	0.0527	0.155
Spectral index above break, δ_2	0.01 – 0.61	0.361	0.403
Convection velocity, v_c [km/(s kpc)]	0 – 10	6.345	6.656
Alfvén velocity, $v_{\text{Alfvén}}$ [km/s]	1 – 30	4.524	8.751
Proton injection spectrum break [MV]	$5 \cdot 10^2 - 1 \cdot 10^5$	$5.195 \cdot 10^2$	$2.986 \cdot 10^3$
Proton spectral index below break, γ_1^p	1.5 – 3.0	1.657	1.999
Proton spectral index above break, γ_2^p	1.5 – 4.5	2.523	2.459
Pulsar spectral index, γ_{psr}	0 – 2.5	1.337	1.394
Pulsar cutoff energy, $E_{\text{cut}}^{\text{psr}}$ [GeV]	$5 \cdot 10^2 - 2 \cdot 10^3$	535.587	559.470
Pulsar formation rate, \dot{N}_{100} [psr/century]	0.161 – 48.61	0.297	0.386
Solar modulation parameter, ϕ_0 [GV]	0.21 – 0.43	0.378	0.370
Solar modulation parameter, ϕ_1 [GV]	1.15 – 1.95	1.950	1.950
Normalization (positrons, protons)	0.5 – 1.5	0.814	0.820
Helium injection spectrum break [MV]	*	$3.053 \cdot 10^5$	$1.361 \cdot 10^4$
Helium spectral index below break, γ_1^{He}	1 – 4	2.505	2.311
Helium spectral index above break, γ_2^{He}	1 – 4	2.425	2.423
Normalization (Helium)	0.5 – 1.5	1.101	1.125

TABLE III. List of free parameters and the parameter ranges, as well as the best-fit values for the fit with positrons, protons and Helium with iMinuit (Step 2) for the default model with a 5.6 kpc halo height and the small-height model with a 3.0 kpc halo height. These models provide a good fit to the data, with a total χ^2 of 88.6 over 141 d.o.f (default model) and 97.08 over 141 d.o.f. (small-height model). Comparing the small-height model to the default model, most parameters remain relatively consistent. However, we required a lower-spectral break for the Helium injection spectrum than allowed in the range of our default model (default model: $5 \cdot 10^4 - 5 \cdot 10^5$ MV, small-height model: $5 \cdot 10^3 - 5 \cdot 10^5$ MV). This model still provides a good fit to the data ($\chi^2/\text{d.o.f.}$ is less than 1). However, the small-height model provides a worse fit ($\Delta\chi^2 = 8.5$) compared to our default model, and thus represents the minimum halo height that appears consistent with AMS-02 data.

For the second step, we take the best-fit values and perform an additional fit by adding the Helium data to the model, using iMinuit. We set the ^4He injection spectrum to follow a twice-broken power-law, with a fixed spectral index below 5 GV of 1.8, and allow the two higher spectral indices and the location of the higher spectral break to float. We allow the normalization of the primary Helium flux to float. We note that there is also a small primary ^3He flux, with a spectrum set to the primary proton spectrum. The relative normalization of these terms, $7.199 \cdot 10^4$ to 9.033, makes the effect of primary ^3He injection negligible. We perform the fit to the Helium data using iMinuit, also allowing the parameters of the previous step to float. As we want to focus on the positron fit of our model, we introduce an additional systematic uncertainty of 2% into the Helium data, accepting that our model does not include several uncertainties that are specific to Helium. More importantly, the systematic uncertainties in the Helium flux are correlated, but here we treat them as uncorrelated.

For the third step, we investigate the dark matter contribution. While we include protons and Helium when fitting our astrophysical background model to the data, to obtain more realistic constraints on the positron flux, we consider the combined (dark matter and astrophysical contribution) to only the positron flux when we set dark matter limits. This always produces more conservative upper limits because dark matter does not directly contribute to the proton or Helium fluxes (leaving the secondary positron contribution approximately the same), and thus the combined (proton+He+positron) χ^2 fit typically provides stronger limits if dark matter induced adjustments to the diffusion parameters perturb these datasets.

To determine the dark matter limits, we study dark matter masses between 5 and 2000 GeV for different annihilation cross sections $\langle\sigma v\rangle$. For each dark matter mass and final state, we set up a grid of annihilation cross sections and fit the model using five parameters that are particularly relevant for the dark matter contribution to the positron flux (D_0 , δ_2) or are degenerate with the dark matter contribution ($E_{\text{cut}}^{\text{psr}}$, γ_{psr} and \dot{N}_{100}), and let them float as well for each grid point. Then we compute the χ^2 profile of $\langle\sigma v\rangle$ and use this to calculate the 95% upper confidence limit compared to a dark matter contribution of zero (*i.e.*, $\chi_{\text{DM}}^2 = \chi_{\text{DM}=0}^2 + 3.84$).

III. RESULTS

In Table III we show the best-fitting parameters of our astrophysical background model to the combined AMS-02 positron, proton and Helium data (Step 2). In general, our best fit parameters for the diffusion coefficients, proton injection spectral indices, convection and Alfvénic velocities and solar modulation parameters are consistent with previous analyses [57, 73–75]. We note that our pulsar formation rate is about an order of magnitude smaller as *e.g.* in Ref. [6]. However, this value depends strongly on the assumptions made about the pulsars (*e.g.*, total spin-down luminosity and initial period), as well as the spectrum, which controls the fraction of the pulsar spin-down power that is injected into the critical 10–1000 GeV range where the pulsar contribution is significant. Several of these parameters (*e.g.*, the total spin-down luminosity) have order of magnitude uncertainties. Another

notable result in our fit is that the break in the proton injection spectrum is positioned at a few GeV, which is very close to the lower limit of our model. This means that a break in the proton injection spectrum is not heavily favored in our model.

In Table IV, we show the resulting fits for both of our models to the combined AMS-02 dataset, as well as the individual fits for each cosmic-ray species. For the default model with a standard halo height of 5.6 kpc, the total χ^2 is 88.60 over 141 degrees of freedom. The χ^2 per degree of freedom for positrons, protons and Helium are 0.88, 0.43, and 0.57, respectively. The $\chi^2/\text{d.o.f.}$ is less than 1 for each model and species, indicating that our model fits the data very well. We note that we treat the systematic uncertainties of nearby energy bins as uncorrelated, even though they are likely to be correlated, which results in an overestimation of the uncertainties and thus a $\chi^2/\text{d.o.f.}$ below 1. The total χ^2 is better in the default model than the small-height model by $\sim 3\sigma$, which means that 3 kpc approximately represents the minimum halo height that is consistent with AMS-02 data.

In Figure 2 we show our best-fit model for positrons, protons and Helium, comparing our results to the AMS-02 data for the best-fit model parameters given in Table III. In the bottom of each plot in Figure 2, we give the residuals ((data-model)/model) of each fit, showing that our model fits the data to within a few percent, providing a very good fit to the cosmic-ray data that are relevant to the positron flux. We observe some systematic uncertainties for low-energy positrons (below 6 GeV) and protons and Helium at higher energies (above 600 GeV). This may correspond to additional secondary proton reacceleration in supernova remnants that is not taken into account in Galprop [75]. Note that the gray shaded regions below 2 GeV and above about 800 GeV, 1050 GeV and 1000 GeV for positrons, protons and Helium, respectively, are not included in the fit. This means that our model has larger uncertainties at energies near these limits.

We point out that our analysis does not take into account the correlation of the systematic uncertainties between nearby energy bins in the AMS-02 data. As can be observed in the residual plots in Figure 2, especially for protons and Helium, the best-fit residual values are highly correlated between nearby energy bins, pointing towards a strong correlation in the systematic uncertainties. We are not able to take these correlations into account because the covariance matrices are not provided by AMS-02, which leads to a miss-estimation of the uncertainties. We additionally note that our calculation of the $\chi^2/\text{d.o.f.}$ for Helium is artificially decreased by the additional 2% systematic error added into the Helium uncertainties. However, we stress that the best-fit value of our parameters, as well as the value of $\Delta\chi^2$ between our models, is preserved in light of these systematic uncertainties.

In Figure 3, the 95% confidence upper limits on the dark matter annihilation cross-sections are presented for the various final decay states. The left panel shows the results of the default model and the right panel the small-height model. We derive the strongest constraints for dark matter annihilation directly into e^+e^- pairs with an annihilation cross section of $6 \cdot 10^{-29} \text{ cm}^3/\text{s}$ for 12.6 GeV in the default model, and an annihilation cross section of $2.6 \cdot 10^{-29} \text{ cm}^3/\text{s}$ for 10.0 GeV in

Halo height	Type	χ^2	$\chi^2/\text{d.o.f.}$ (d.o.f.)
5.6 kpc	total	88.60	0.63 (141)
	positrons	42.88	0.88 (49)
	protons	21.08	0.43 (49)
	Helium	24.64	0.57 (43)
3 kpc	total	97.08	0.69 (141)
	positrons	47.70	0.97 (49)
	protons	18.97	0.39 (49)
	Helium	30.41	0.71 (43)

TABLE IV. The χ^2 -values and χ^2 per degree of freedom of the iMinit fit for the total flux and the individual fluxes for positrons, protons and Helium. Values for the default model are given in the top rows and for the small-height model in the bottom rows.

the small-height model, both of which lie below the thermal annihilation cross section by about 3 orders of magnitude.

Our limits show a small bump at low energies for all final states. Specifically, in the default model for the $\tau^+\tau^-$ final state, the bump peaks at 10 GeV with a local significance of 2.8σ , for $\mu^+\mu^-$ the peak is at 8 GeV with a local significance of 2.9σ , for $e^+e^-e^+e^-$ the peak is at 6.3 GeV with a local significance of 2.8σ , and for e^+e^- the peak is at 5 GeV with a local significance of 3.1σ . In the small-height model, for $\tau^+\tau^-$ the excess peaks at 13 GeV and 2.7σ , for $\mu^+\mu^-$ at 8 GeV and 3.9σ , for $e^+e^-e^+e^-$ at 6 GeV and 3.6σ and for e^+e^- at 5 GeV and 3.6σ . These all correspond to the same spectral feature in the low energy positron fit of our model, which can be seen in Figure 2 as a positive discrepancy (about 2%) between our model and the AMS-02 data below about 5 GeV. We note that this region of our model is prone to larger uncertainties, as these energies are close to the lower limit of our model (2 GeV). Additionally, lower energies are highly affected by uncertainties in solar modulation.

IV. DISCUSSION AND CONCLUSIONS

In this paper, we calculated constraints on the dark matter annihilation cross section for dark matter masses between 5 and 2000 GeV for leptonic final states using the local positron flux. We exclude the thermal cross-section for annihilation into $\tau^+\tau^-$ below 60 GeV, for $\mu^+\mu^-$ below 160 GeV, for $e^+e^-e^+e^-$ below 240 GeV and for e^+e^- below 380 GeV for our default model with a halo height of 5.6 kpc.

We repeated our analysis with a conservative halo height of 3 kpc in the small-height model, for which we obtain similar constraints: Our limits are below the thermal cross section for annihilation into $\tau^+\tau^-$ below 50 GeV, for $\mu^+\mu^-$ below 170 GeV, for $e^+e^-e^+e^-$ below 430 GeV and for e^+e^- below 500 GeV. We note that our constraints at higher energies are stronger in the small-height model than the default model. This is because our two models have a different diffusion coefficient at high energies, meaning that the diffusion distance is slightly longer in the small-height model which results in the stronger constraints at high masses ($\gtrsim 300$ GeV). We conclude from our results that a change in halo height does not significantly affect the local positron flux, contrary to limits on

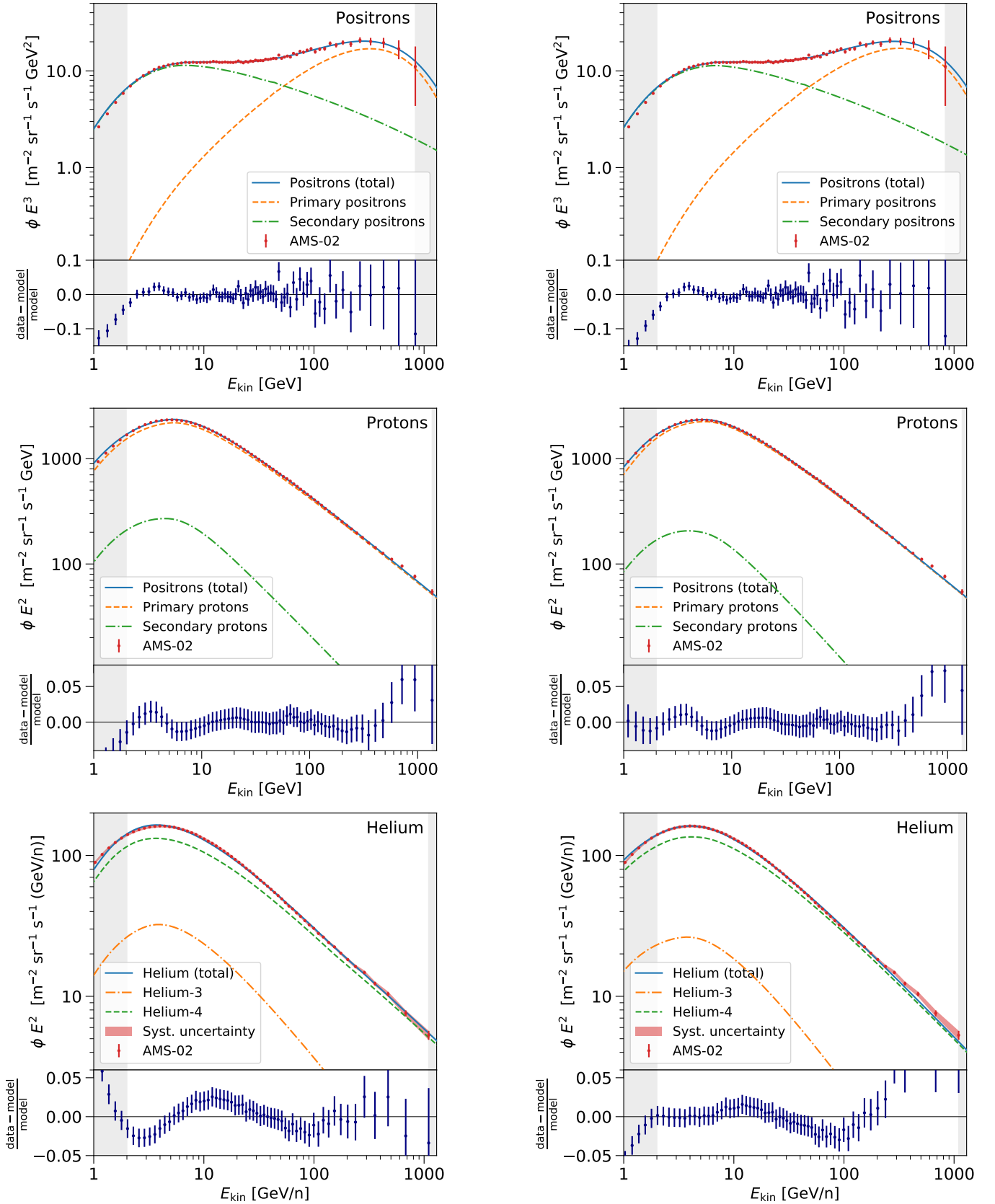


FIG. 2. The astrophysical model for positrons (top), protons (middle), and Helium (bottom), plotted in solid blue lines, together with the data from AMS-02 for positrons [5], protons [41, 42] and Helium [43], displayed in red. The left panels show the default model (5.6 kpc halo height) and the right panels the small-height model (3 kpc halo height). For positrons and protons, primary components are displayed in orange (dashed), secondary components in green (dashed-dotted). ^3He and ^4He are represented by orange (dashed-dotted) and green (dashed), respectively. Note also that the Helium fit includes an additional systematic uncertainty band of 2%. Gray shaded regions are excluded from the fit. The fractional residuals of the fits are given at the bottom of each panel, showing that we fit all data to a few percent accuracy.

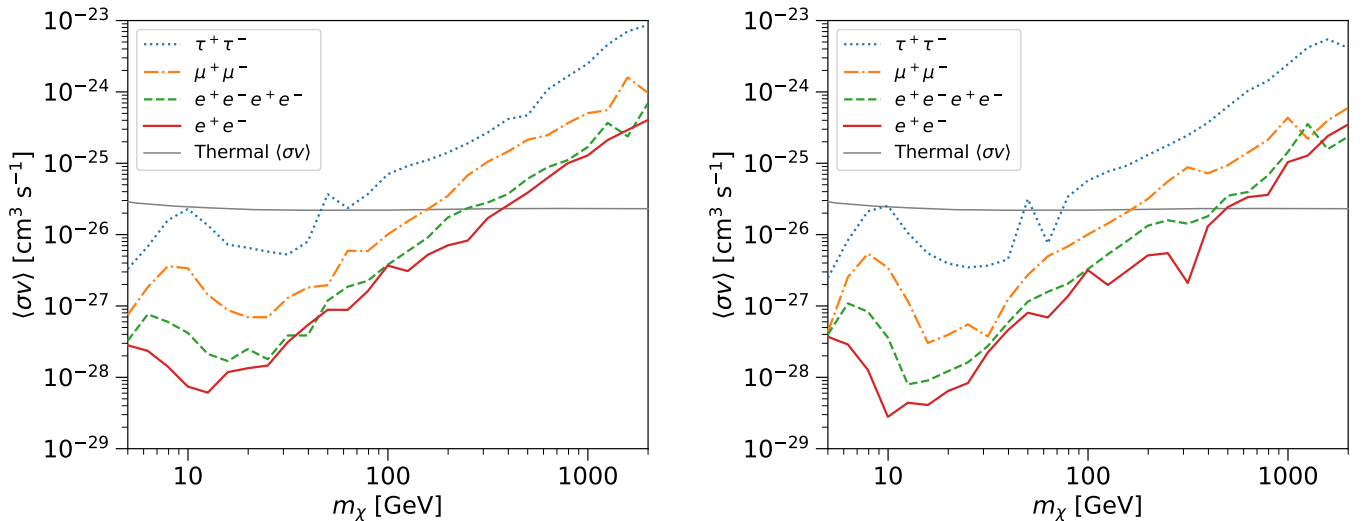


FIG. 3. Dark matter limits for different leptophilic final states for a dark matter mass range from 5 to 2000 GeV, for a halo height of 5.6 kpc (left) in the default model and 3 kpc (right) in the small-height model, for decays into $\tau^+\tau^-$ (blue, dotted), $\mu^+\mu^-$ (orange, dashed-dotted), $e^+e^-e^+e^-$ (green, dashed) and e^+e^- (red, solid). The thermal cross section (gray, solid) is taken from [76]. Our limits rule out a thermal annihilation cross section for dark matter masses below between 60 to 300 GeV in the default model and between 60 and 500 GeV in the small-height model, depending on the final state.

the local antiproton flux that depends on the halo height [57]. This is due to the fact that the average positron travels a shorter distance than antiprotons at similar energy (because their energy losses are faster) – making the edges of the diffusion zone less important for leptonic dark matter limits.

Our analysis improves on the constraints by Bergström *et al.* by about a factor of 2 for both models. This is despite the fact that our model gives significantly more freedom to the astrophysical background fit – and thus includes more conservative and robust limits. Note that Bergström *et al.* use a halo height of 4 kpc. We are also able to extend the limits up to dark matter masses of 2000 GeV as more cosmic-ray data is available at higher energies.

Our limits also set strong constraints on dark matter models with only subdominant annihilations into the four leptonic final states considered in this work. At about 30 GeV, our limits fall below the thermal cross section by about two orders of magnitude for annihilation into e^+e^- . This means that our limits even rule out subdominant contributions from dark matter annihilations (*i.e.*, $\sim 1\%$ annihilation into e^+e^- pairs at 30 GeV), and similarly $\sim 10\%$ for annihilations into $\mu^+\mu^-$. Notably, dark matter models with significant annihilation fractions into $\mu^+\mu^-$ final states are among the most difficult thermal dark matter models to constrain with current experiments [77]. Compared to the results of Ref. [77], which only ruled out thermal annihilation to $\mu^+\mu^-$ up to a dark matter mass of 30 GeV, we rule out annihilation to $\mu^+\mu^-$ up to masses of ~ 150 GeV. We note that a significant fraction of this difference pertains to less conservative model assumptions utilized in this work, compared to that of Ref. [77]. For example, they use a local dark matter density of 0.25 GeV/cm^3 and local magnetic field strength of $8.9 \mu\text{G}$, both of which serve to significantly decrease the local positron flux from dark matter

at a given annihilation cross-section. On the other hand, our limits benefit from the use of a physical model for the astrophysical contributions from pulsars and secondary production, rather than producing an empirical fit to the data. Our limits also profit from the better data by AMS-02, which dominates the improvement of our limits at higher energies. Thus our results can also improve generic constraints on dark matter annihilation to mixed final states.

Our limits are highly complementary with γ -ray constraints on dark matter annihilation. In particular, direct annihilations to e^+e^- , $\mu^+\mu^-$ and light mediator final states are difficult to probe with γ -ray instruments, because their decays produce few γ -rays at tree-level. On the other hand, γ -ray studies are highly sensitive to dark matter annihilation into hadronic final states, which are not tested here. Our limits, in conjunction with current limits on dark matter annihilation to hadronic states (*e.g.*, in dwarf spheroidal galaxies) place strong limits on dark matter annihilation regardless of final state.

ACKNOWLEDGEMENTS

We thank John Beacom, Ilias Cholis, Carmelo Evoli, Andrei Kounine and Rebecca Leane for comments that improved the quality of this paper. We would like to especially thank Michael Korsmeier for numerous comments and discussions regarding the production of our astrophysical models. TL is supported by the Swedish Research Council under contract 2019-05135, the Swedish National Space Agency under contract 117/19 and the European Research Council under grant 742104. This project used computing resources from the Swedish National Infrastructure for Computing (SNIC) under project Nos. 2020/5-463 and 2021-1-24 partially funded by the Swedish Research Council through grant no. 2018-05973.

- [1] Webpage. <https://ams02.space/>.
- [2] O. Adriani *et al.* (PAMELA), *Phys. Rev. Lett.* **105**, 121101 (2010), arXiv:1007.0821 [astro-ph.HE].
- [3] S. W. Barwick *et al.* (HEAT), *Astrophys. J. Lett.* **482**, L191 (1997), arXiv:astro-ph/9703192.
- [4] R. L. Golden, B. G. Mauger, S. Horan, S. A. Stephens, R. R. Daniel, G. D. Badhwar, J. L. Lacy, and J. E. Zipse, *A&A* **188**, 145 (1987).
- [5] M. Aguilar, L. Ali Cavazonza, G. Ambrosi, L. Arruda, N. Attig, P. Azzarello, A. Bachlechner, F. Barao, and et. al. (AMS Collaboration), *Phys. Rev. Lett.* **122**, 041102 (2019).
- [6] D. Hooper, P. Blasi, and P. D. Serpico, *JCAP* **01**, 025 (2009), arXiv:0810.1527 [astro-ph].
- [7] S. Profumo, *Central Eur. J. Phys.* **10**, 1 (2011), arXiv:0812.4457 [astro-ph].
- [8] T. Linden and S. Profumo, *Astrophys. J.* **772**, 18 (2013), arXiv:1304.1791 [astro-ph.HE].
- [9] H. Yuksel, M. D. Kistler, and T. Stanev, *Phys. Rev. Lett.* **103**, 051101 (2009), arXiv:0810.2784 [astro-ph].
- [10] D. Malyshev, I. Cholis, and J. Gelfand, *Phys. Rev. D* **80**, 063005 (2009), arXiv:0903.1310 [astro-ph.HE].
- [11] M. S. Turner and F. Wilczek, *Phys. Rev. D* **42**, 1001 (1990).
- [12] N. Arkani-Hamed, D. P. Finkbeiner, T. R. Slatyer, and N. Weiner, *Phys. Rev. D* **79**, 015014 (2009), arXiv:0810.0713 [hep-ph].
- [13] I. Cholis and D. Hooper, *Phys. Rev. D* **88**, 023013 (2013), arXiv:1304.1840 [astro-ph.HE].
- [14] L. Bergstrom, T. Bringmann, and J. Edsjo, *Phys. Rev. D* **78**, 103520 (2008), arXiv:0808.3725 [astro-ph].
- [15] M. Cirelli and A. Strumia, *PoS IDM2008*, 089 (2008), arXiv:0808.3867 [astro-ph].
- [16] I. Cholis, L. Goodenough, D. Hooper, M. Simet, and N. Weiner, *Phys. Rev. D* **80**, 123511 (2009), arXiv:0809.1683 [hep-ph].
- [17] M. Cirelli, M. Kadastik, M. Raidal, and A. Strumia, *Nucl. Phys. B* **813**, 1 (2009), [Addendum: *Nucl. Phys. B* 873, 530–533 (2013)], arXiv:0809.2409 [hep-ph].
- [18] I. Cholis, D. P. Finkbeiner, L. Goodenough, and N. Weiner, *JCAP* **12**, 007 (2009), arXiv:0810.5344 [astro-ph].
- [19] I. Cholis, G. Dobler, D. P. Finkbeiner, L. Goodenough, and N. Weiner, *Phys. Rev. D* **80**, 123518 (2009), arXiv:0811.3641 [astro-ph].
- [20] A. U. Abeysekara *et al.*, *Astrophys. J.* **843**, 40 (2017), arXiv:1702.02992 [astro-ph.HE].
- [21] T. Linden, K. Auchettl, J. Bramante, I. Cholis, K. Fang, D. Hooper, T. Karwal, and S. W. Li, *Phys. Rev. D* **96**, 103016 (2017), arXiv:1703.09704 [astro-ph.HE].
- [22] A. U. Abeysekara *et al.* (HAWC), *Science* **358**, 911 (2017), arXiv:1711.06223 [astro-ph.HE].
- [23] H. Abdalla *et al.* (HESS), *Astron. Astrophys.* **612**, A1 (2018), arXiv:1804.02432 [astro-ph.HE].
- [24] M. Di Mauro, S. Manconi, and F. Donato, *Phys. Rev. D* **101**, 103035 (2020), arXiv:1908.03216 [astro-ph.HE].
- [25] T. Sudoh, T. Linden, and J. F. Beacom, *Phys. Rev. D* **100**, 043016 (2019), arXiv:1902.08203 [astro-ph.HE].
- [26] G. Johannesson, T. A. Porter, and I. V. Moskalenko, *Astrophys. J.* **879**, 91 (2019), arXiv:1903.05509 [astro-ph.HE].
- [27] T. Sudoh, T. Linden, and D. Hooper, (2021), arXiv:2101.11026 [astro-ph.HE].
- [28] D. Grasso, S. Profumo, A. Strong, L. Baldini, R. Bellazzini, E. Bloom, J. Bregeon, G. Di Bernardo, D. Gaggero, N. Giglietto, and et al., *Astroparticle Physics* **32**, 140–151 (2009).
- [29] D. Hooper, I. Cholis, T. Linden, and K. Fang, *Phys. Rev. D* **96**, 103013 (2017), arXiv:1702.08436 [astro-ph.HE].
- [30] D. Hooper and T. Linden, *Phys. Rev. D* **98**, 083009 (2018), arXiv:1711.07482 [astro-ph.HE].
- [31] K. Fang, X.-J. Bi, P.-F. Yin, and Q. Yuan, *Astrophys. J.* **863**, 30 (2018), arXiv:1803.02640 [astro-ph.HE].
- [32] S. Profumo, J. Reynoso-Cordova, N. Kaaz, and M. Silverman, *Phys. Rev. D* **97**, 123008 (2018), arXiv:1803.09731 [astro-ph.HE].
- [33] S. Manconi, M. Di Mauro, and F. Donato, *Phys. Rev. D* **102**, 023015 (2020), arXiv:2001.09985 [astro-ph.HE].
- [34] M. Ackermann, M. Ajello, A. Albert, W. B. Atwood, L. Baldini, J. Ballet, G. Barbiellini, D. Bastieri, K. Bechtol, R. Bellazzini, and et al., *Physical Review Letters* **107** (2011), 10.1103/physrevlett.107.241302.
- [35] A. Geringer-Sameth and S. M. Koushiappas, *Physical Review Letters* **107** (2011), 10.1103/physrevlett.107.241303.
- [36] I. Cholis and P. Salucci, *Physical Review D* **86** (2012), 10.1103/physrevd.86.023528.
- [37] S. Hoof, A. Geringer-Sameth, and R. Trotta, *Journal of Cosmology and Astroparticle Physics* **2020**, 012–012 (2020).
- [38] A. Albert, B. Anderson, K. Bechtol, A. Drlica-Wagner, M. Meyer, M. Sánchez-Conde, L. Strigari, M. Wood, T. M. C. Abbott, F. B. Abdalla, and et al., *The Astrophysical Journal* **834**, 110 (2017).
- [39] M. Ackermann, A. Albert, B. Anderson, W. Atwood, L. Baldini, G. Barbiellini, D. Bastieri, K. Bechtol, R. Bellazzini, E. Bissaldi, and et al., *Physical Review Letters* **115** (2015), 10.1103/physrevlett.115.231301.
- [40] L. Bergstrom, T. Bringmann, I. Cholis, D. Hooper, and C. Weniger, *Phys. Rev. Lett.* **111**, 171101 (2013), arXiv:1306.3983 [astro-ph.HE].
- [41] M. Aguilar, L. Ali Cavazonza, B. Alpat, G. Ambrosi, L. Arruda, N. Attig, S. Aupetit, P. Azzarello, and et al. (AMS Collaboration), *Phys. Rev. Lett.* **121**, 051101 (2018).
- [42] M. Aguilar, D. Aisa, B. Alpat, A. Alvino, G. Ambrosi, K. Andeen, L. Arruda, N. Attig, and et al. (AMS Collaboration), *Phys. Rev. Lett.* **114**, 171103 (2015).
- [43] M. Aguilar, D. Aisa, B. Alpat, A. Alvino, G. Ambrosi, K. Andeen, L. Arruda, N. Attig, and et al. (AMS Collaboration), *Phys. Rev. Lett.* **115**, 211101 (2015).
- [44] “Galprop,” <https://galprop.stanford.edu/>.
- [45] I. Cholis, D. Hooper, and T. Linden, (2020), arXiv:2007.00669 [astro-ph.HE].
- [46] L. Gleeson and W. Axford, *Astrophys. J.* **154**, 1011 (1968).
- [47] M. Aguilar, L. Ali Cavazonza, G. Ambrosi, L. Arruda, N. Attig, A. Bachlechner, F. Barao, A. Barrau, and et al. (AMS Collaboration), *Phys. Rev. Lett.* **123**, 181102 (2019).
- [48] A. W. Strong and I. V. Moskalenko, *Astrophys. J.* **509**, 212 (1998), arXiv:astro-ph/9807150.
- [49] A. W. Strong and I. V. Moskalenko, in *26th International Cosmic Ray Conference*, Vol. 4 (1999) p. 255, arXiv:astro-ph/9906228.
- [50] A. W. Strong and I. V. Moskalenko, *Adv. Space Res.* **27**, 717 (2001), arXiv:astro-ph/0101068.
- [51] A. W. Strong, I. V. Moskalenko, T. A. Porter, G. Johannesson, E. Orlando, and S. W. Digel, (2009), arXiv:0907.0559 [astro-ph.HE].
- [52] I. V. Moskalenko and A. W. Strong, *Astrophys. J.* **493**, 694 (1998), arXiv:astro-ph/9710124.

- [53] I. V. Moskalenko and A. W. Strong, in *26th International Cosmic Ray Conference*, Vol. 2 (1999) p. 320, arXiv:astro-ph/9906230.
- [54] E. Orlando, G. Jóhannesson, I. V. Moskalenko, T. A. Porter, and A. Strong, *Nucl. Part. Phys. Proc.* **297-299**, 129 (2018), arXiv:1712.09755 [astro-ph.HE].
- [55] G. Jóhannesson, I. V. Moskalenko, E. Orlando, T. Porter, and A. Strong, *PoS ICRC2015*, 517 (2016).
- [56] R. Diehl *et al.*, *Nature* **439**, 45 (2006), arXiv:astro-ph/0601015.
- [57] M. Korsmeier and A. Cuoco, (2021), arXiv:2103.09824 [astro-ph.HE].
- [58] N. Weinrich, M. Boudaud, L. Derome, Y. Genolini, J. Lavalle, D. Maurin, P. Salati, P. Serpico, and G. Weymann-Despres, *Astron. Astrophys.* **639**, A74 (2020), arXiv:2004.00441 [astro-ph.HE].
- [59] C. Evoli, G. Morlino, P. Blasi, and R. Aloisio, *Phys. Rev. D* **101**, 023013 (2020), arXiv:1910.04113 [astro-ph.HE].
- [60] D. R. Lorimer, *IAU Symp.* **218**, 105 (2004), arXiv:astro-ph/0308501.
- [61] D. Lorimer *et al.*, *Mon. Not. Roy. Astron. Soc.* **372**, 777 (2006), arXiv:astro-ph/0607640.
- [62] M. Ackermann *et al.* (Fermi-LAT), *Astrophys. J.* **799**, 86 (2015), arXiv:1410.3696 [astro-ph.HE].
- [63] J. I. Read, *J. Phys. G* **41**, 063101 (2014), arXiv:1404.1938 [astro-ph.GA].
- [64] J. F. Navarro, C. S. Frenk, and S. D. M. White, *Astrophys. J.* **462**, 563 (1996), arXiv:astro-ph/9508025.
- [65] P. Gondolo, J. Edsjo, P. Ullio, L. Bergstrom, M. Schelke, and E. A. Baltz, *JCAP* **07**, 008 (2004), arXiv:astro-ph/0406204.
- [66] J.-F. Fortin, J. Shelton, S. Thomas, and Y. Zhao, (2009), arXiv:0908.2258 [hep-ph].
- [67] Webpage. <https://johannesbuchner.github.io/PyMultiNest/>.
- [68] F. Feroz and M. P. Hobson, *Mon. Not. Roy. Astron. Soc.* **384**, 449 (2008), arXiv:0704.3704 [astro-ph].
- [69] F. Feroz, M. P. Hobson, and M. Bridges, *Mon. Not. Roy. Astron. Soc.* **398**, 1601 (2009), arXiv:0809.3437 [astro-ph].
- [70] F. Feroz, M. P. Hobson, E. Cameron, and A. N. Pettitt, *Open J. Astrophys.* **2**, 10 (2019), arXiv:1306.2144 [astro-ph.IM].
- [71] Webpage. <https://iminuit.readthedocs.io/en/stable/>.
- [72] H. Dembinski and P. O. et al., (2020), 10.5281/zenodo.4310361.
- [73] R. Trotta, G. Jóhannesson, I. V. Moskalenko, T. A. Porter, R. R. d. Austri, and A. W. Strong, *Astrophys. J.* **729**, 106 (2011), arXiv:1011.0037 [astro-ph.HE].
- [74] G. Jóhannesson *et al.*, *Astrophys. J.* **824**, 16 (2016), arXiv:1602.02243 [astro-ph.HE].
- [75] I. Cholis, D. Hooper, and T. Linden, *Phys. Rev. D* **95**, 123007 (2017), arXiv:1701.04406 [astro-ph.HE].
- [76] G. Steigman, B. Dasgupta, and J. F. Beacom, *Phys. Rev. D* **86**, 023506 (2012), arXiv:1204.3622 [hep-ph].
- [77] R. K. Leane, T. R. Slatyer, J. F. Beacom, and K. C. Y. Ng, *Phys. Rev. D* **98**, 023016 (2018), arXiv:1805.10305 [hep-ph].

Appendix A: Astrophysical model with Multinest

In this section, we present the results from the first step of creating our astrophysical background models, in which we fit our Galprop model to the AMS-02 data for positrons and protons (see Table I for the specific AMS-02 data sets) with Multinest [67], *i.e.*, we do not fit the Helium spectrum in this step. We choose to include this step because Multi-

Halo height	Type	χ^2	$\chi^2/\text{d.o.f. (d.o.f.)}$
5.6 kpc	total	61.54	0.61 (101)
	positrons	39.41	0.76 (52)
	protons	22.13	0.45 (49)
3 kpc	total	63.24	0.63 (101)
	positrons	41.22	0.79 (52)
	protons	22.02	0.45 (49)

TABLE V. Summary of the χ^2 -values of the Multinest fit for the default model (halo height 5.6 kpc, top rows) and the small-height model (halo height 3 kpc, bottom rows) for the total flux, as well as the individual positron and proton flux. All χ^2 per degree of freedom are below 1, indicating very good agreement of our astrophysical model with the AMS-02 data.

nest is very reliable at finding the global minimum of the fit, whereas iMinuit is more likely to fall into local minima in large multi-dimensional parameter spaces. The free parameters can be found in Tables VI and VII for the default and small-height model, respectively, and include the following parameters: the diffusion spectrum, the proton injection spectrum (with a spectral break and a spectral index below and above the break), the convection velocity, the Alfvén velocity, the Galactic pulsar formation rate and spectrum (with a spectral index and energy cutoff), the solar modulation parameters and an overall normalization of the primary particle abundance of $1.06 \cdot 10^6$ for protons in Galprop.

We present our results in Tables VI and VII for the default and small-height model, respectively, where we give the range in which we allow the parameters to float, the type of prior (*i.e.*, linear or logarithmic), the best-fit value, the posterior value and the posterior uncertainty. In particular, we scan the priors for D_0 , D_{break} , the proton injection spectral break and $E_{\text{cut}}^{\text{psr}}$ in logarithmic space, while we use a flat distribution for the other parameters. We obtain results that are relatively consistent between the default and small-height model.

Figure 4 shows our fit for positrons and protons for our default model and the small-height model, together with the AMS-02 data for the local fluxes. The fractional residuals between the data and our model are given in the bottom of each panel, showing that our models fit the AMS-02 data to within a few percent for the data that is relevant to the positron flux.

A summary of the χ^2 -values is given in Table V for the default model and small-height model. For the default model, the total χ^2 is 61.5 over 101 degrees of freedom, with $\chi_p^2/\text{d.o.f.} = 0.45$ and $\chi_{e^+}^2/\text{d.o.f.} = 0.76$. For the small-height model, the total χ^2 is 63.2 over 101 degrees of freedom, with $\chi_p^2/\text{d.o.f.} = 0.45$ and $\chi_{e^+}^2/\text{d.o.f.} = 0.79$.

The best-fit values (rather than the posterior means) obtained in this step serve as the initial values for the iMinuit fit in the second step, allowing us to start the fitting procedure close to the global minimum. Comparing our Multinest fit with the second iMinuit fit (see Table III), we remark that the positron and proton fit only worsen slightly ($\Delta\chi^2/\text{d.o.f.} \approx 0.04$) when introducing the fit to the Helium data in the default model. In the small-height model, $\Delta\chi^2/\text{d.o.f.} \approx 0.18$ for positrons, while the proton fit improves by $\Delta\chi^2/\text{d.o.f.} \approx 0.06$.

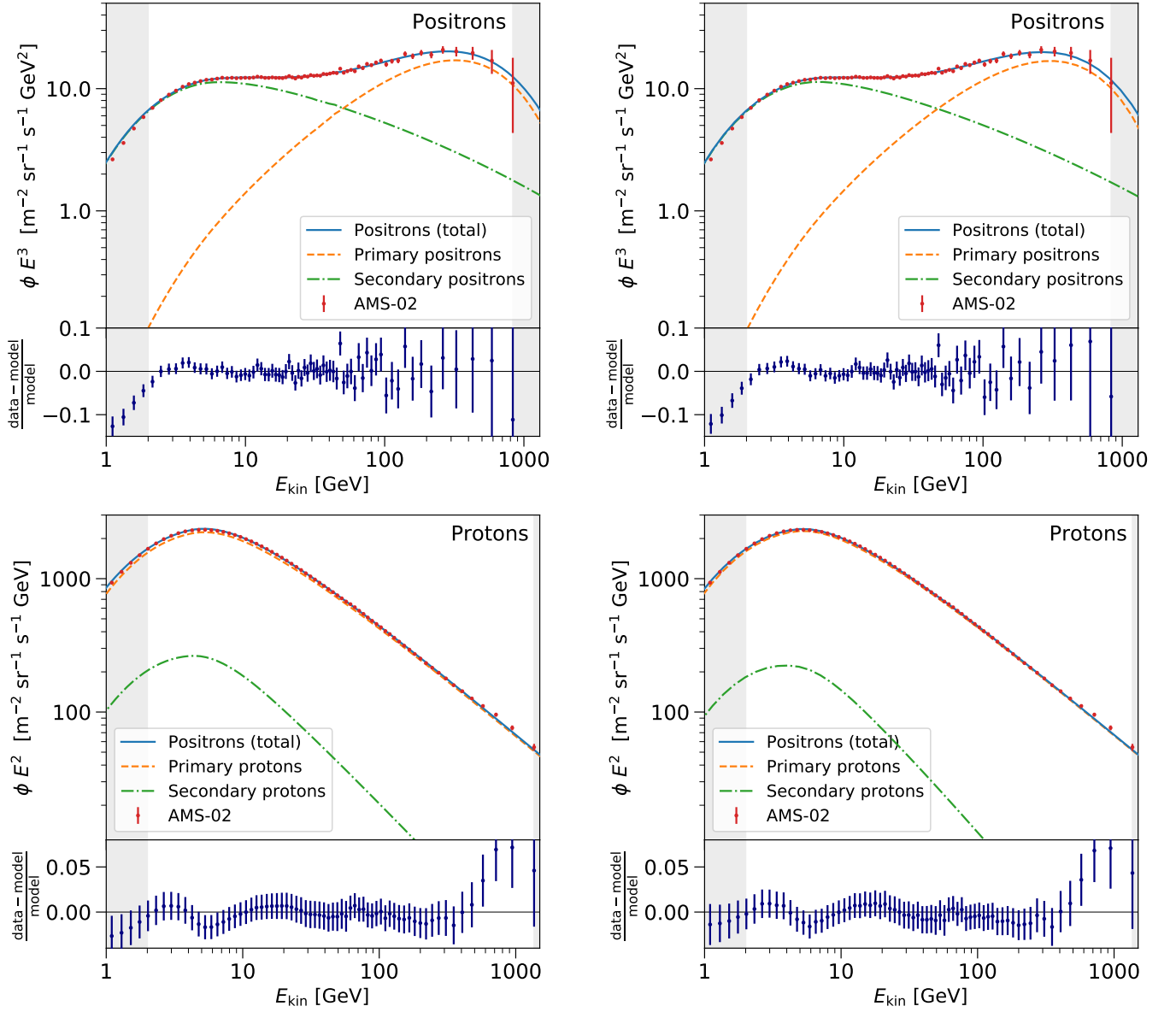


FIG. 4. Astrophysical model obtained with Multinest for the local flux of positrons (top panels) and protons (bottom panels). Gray shaded regions are excluded when fitting the model to the data. The left panels show the default model ($z = 5.6$ kpc), and the right panels show the small-height model ($z = 3$ kpc). The AMS-02 data is given in red for positrons [5] and protons [41, 42]. The total flux of our model is presented in blue (solid), primary components in orange (dashed) and secondary components in green (dashed-dotted). The fractional residuals between the data and our model are given in the bottom of each panel, showing that our models for positrons and protons fit the data to a few percent accuracy for both halo heights.

Parameter	Range	Prior	Best fit	Posterior	Posterior uncertainty
Diffusion coefficient, D_0 [cm^2/s]	$10^{28} - 10^{30}$	log	$1.563 \cdot 10^{28}$	$1.732 \cdot 10^{28}$	$1.026 \cdot 10^{28}$
Break in diffusion spectrum, D_{break} [MV]	$10^3 - 1.4 \cdot 10^4$	log	$5.479 \cdot 10^3$	$5.758 \cdot 10^3$	$0.283 \cdot 10^3$
Spectral index below break, δ_1	0.01 – 0.61	linear	0.053	0.047	0.017
Spectral index above break, δ_2	0.01 – 0.61	linear	0.364	0.383	0.027
Convection velocity, v_c [km/(s kpc)]	0 – 10	linear	7.282	6.7	2.0
Alfvén velocity, $v_{\text{Alfvén}}$ [km/s]	1 – 30	linear	4.553	4.2	1.0
Proton injection spectrum break [MV]	$5 \cdot 10^2 - 1 \cdot 10^5$	log	$2.064 \cdot 10^3$	$1.389 \cdot 10^3$	$0.787 \cdot 10^3$
Proton spectral index below break, γ_1^p	1.5 – 3.0	linear	2.196	2.12	0.39
Proton spectral index above break, γ_2^p	1.5 – 4.5	linear	2.535	2.510	0.023
Pulsar spectral index, γ_{psr}	0 – 2.5	linear	1.374	1.480	0.051
Pulsar cutoff energy, $E_{\text{cut}}^{\text{psr}}$ [GeV]	$5 \cdot 10^2 - 2 \cdot 10^3$	log	554.341	714	118
Pulsar formation rate, \dot{N}_{100} [psr/century]	0.148 – 44.40	linear	0.297	0.497	0.132
Solar modulation parameter, ϕ_0 [GV]	0.21 – 0.43	linear	0.386	0.366	0.012
Solar modulation parameter, ϕ_1 [GV]	1.15 – 1.95	linear	1.501	1.64	0.23
Normalization (positrons, protons)	0.5 – 1.5	linear	0.818	0.8206	0.0038

TABLE VI. List of free parameters of our Multinest fit for the default model ($z = 5.6$ kpc). We give the range in which we let the parameters float, the type of prior, the best-fit value, the posterior and the posterior uncertainty. This model provides a good fit to the data with a total χ^2 of 61.54 over 101 degrees of freedom.

Parameter	Range	Prior	Best fit	Posterior	Posterior uncertainty
Diffusion coefficient, D_0 [cm^2/s]	$10^{28} - 10^{30}$	log	$1.822 \cdot 10^{28}$	$1.994 \cdot 10^{28}$	$1.316 \cdot 10^{28}$
Break in diffusion spectrum, D_{break} [MV]	$10^3 - 1.4 \cdot 10^4$	log	$5.938 \cdot 10^3$	$6.026 \cdot 10^3$	$0.371 \cdot 10^3$
Spectral index below break, δ_1	0.01 – 0.61	linear	0.147	0.123	0.038
Spectral index above break, δ_2	0.01 – 0.61	linear	0.430	0.460	0.037
Convection velocity, v_c [km/(s kpc)]	0 – 10	linear	6.724	2.4	2.0
Alfvén velocity, $v_{\text{Alfvén}}$ [km/s]	1 – 30	linear	9.148	6.8	1.4
Proton injection spectrum break [MV]	$5 \cdot 10^2 - 1 \cdot 10^5$	log	$1.649 \cdot 10^3$	$1.335 \cdot 10^3$	$0.841 \cdot 10^3$
Proton spectral index below break, γ_1^p	1.5 – 3.0	linear	1.546	2.19	0.43
Proton spectral index above break, γ_2^p	1.5 – 4.5	linear	2.429	2.389	0.034
Pulsar spectral index, γ_{psr}	0 – 2.5	linear	1.398	1.487	0.057
Pulsar cutoff energy, $E_{\text{cut}}^{\text{psr}}$ [GeV]	$5 \cdot 10^2 - 2 \cdot 10^3$	log	506.825	640	108
Pulsar formation rate, \dot{N}_{100} [psr/century]	0.148 – 44.40	linear	0.351	0.479	0.171
Solar modulation parameter, ϕ_0 [GV]	0.21 – 0.43	linear	0.403	0.377	0.023
Solar modulation parameter, ϕ_1 [GV]	1.15 – 1.95	linear	1.402	1.54	0.26
Normalization (positrons, protons)	0.5 – 1.5	linear	0.824	0.8266	0.0037

TABLE VII. Same as Table VI, but for the small-height model ($z = 3$ kpc). This model provides a good fit to the data, with a χ^2 of 63.24 over 101 degrees of freedom. The results are relatively consistent with the default model.